2024

Impacts of Carbonate Buffering on Atmospheric Equilibration of CO2, δ13CDIC, and Δ14CDIC in Rivers and Streams

Matthew J. Winnick

Brian Saccardi

Recommended Citation

Winnick, Matthew J. and Saccardi, Brian, "Impacts of Carbonate Buffering on Atmospheric Equilibration of CO2, δ13CDIC, and Δ14CDIC in Rivers and Streams" (2024). *Global Biochemical Cycles*. 40.
https://doi.org/10.1029/2023GB007860

Global Biogeochemical Cycles

RESEARCH ARTICLE

10.1029/2023GB007860

Key Points:

- We develop models of stream CO_2 degassing that include carbonate buffering and apply them across a range of alkalinities and stream processes
- Carbonate buffering can support significant contributions to stream CO_2 fluxes but cannot support elevated downstream CO_2 concentrations
- Stable and radio- carbon isotopes are decoupled from CO_2 by carbonate buffering but can be leveraged to partition carbon sources

Supporting Information:

Supporting Information may be found in the online version of this article.

Correspondence to:

M. J. Winnick,
mwinnick@umass.edu

Citation:

Winnick, M. J., & Saccardi, B. (2024). Impacts of carbonate buffering on atmospheric equilibration of CO_2, $\delta^{13}C_{DIC}$, and $\Delta^{14}C_{DIC}$ in rivers and streams. *Global Biogeochemical Cycles*, *38*, e2023GB007860. https://doi.org/10.1029/2023GB007860

Received 26 MAY 2023
Accepted 25 JAN 2024

Author Contributions:

Conceptualization: Matthew J. Winnick
Formal analysis: Matthew J. Winnick
Funding acquisition: Matthew J. Winnick
Methodology: Matthew J. Winnick, Brian Saccardi
Software: Matthew J. Winnick, Brian Saccardi
Visualization: Matthew J. Winnick
Writing – original draft: Matthew J. Winnick

Impacts of Carbonate Buffering on Atmospheric Equilibration of CO_2, $\delta^{13}C_{DIC}$, and $\Delta^{14}C_{DIC}$ in Rivers and Streams

Matthew J. Winnick[1] and **Brian Saccardi**[1]

[1]Department of Earth, Geographic, and Climate Sciences, University of Massachusetts Amherst, Amherst, MA, USA

Abstract

Rivers and streams play an important role within the global carbon cycle, in part through emissions of carbon dioxide (CO_2) to the atmosphere. However, the sources of this CO_2 and their spatiotemporal variability are difficult to constrain. Recent work has highlighted the role of carbonate buffering reactions that may serve as a source of CO_2 in high alkalinity systems. In this study, we seek to develop a quantitative framework for the role of carbonate buffering in the fluxes and spatiotemporal patterns of CO_2 and the stable and radio- isotope composition of dissolved inorganic carbon (DIC). We incorporate DIC speciation calculations of carbon isotopologues into a stream network CO_2 model and perform a series of simulations, ranging from the degassing of a groundwater seep to a hydrologically-coupled 5th-order stream network. We find that carbonate buffering reactions contribute >60% of emissions in high-alkalinity, moderate groundwater-CO_2 environments. However, atmosphere equilibration timescales of CO_2 are minimally affected, which contradicts hypotheses that carbonate buffering maintains high CO_2 across Strahler orders in high alkalinity systems. In contrast, alkalinity dramatically increases isotope equilibration timescales, which acts to decouple CO_2 and DIC variations from the isotopic composition even under low alkalinity. This significantly complicates a common method for carbon source identification. Based on similar impacts on atmospheric equilibration for stable and radio- carbon isotopologues, we develop a quantitative method for partitioning groundwater and stream corridor carbon sources in carbonate-dominated watersheds. Together, these results provide a framework to guide fieldwork and interpretations of stream network CO_2 patterns across variable alkalinities.

Plain Language Summary

Streams emit a lot of carbon dioxide (CO_2) to the atmosphere, but it is difficult to figure out where the CO_2 originates. One source is a chemical reaction called carbonate buffering, which happens between different forms of dissolved inorganic carbon. This reaction may be important in streams with high alkalinity, but we lack knowledge about how it contributes across different alkalinities and scales. Some studies use isotopes of carbon to trace where CO_2 comes from and how it is released, but we lack knowledge about how carbonate buffering affects isotope patterns. Here, we create mathematical models of CO_2 production and release, including isotopes in streams. Our findings show that carbonate buffering can be a significant source of CO_2 in streams with high alkalinity. However, it doesn't keep CO_2 levels consistently high downstream, as studies previously suggested. Conversely, carbonate buffering has a big effect on the patterns of carbon isotopes. This means that common isotope methods for identifying stream CO_2 sources don't work well. Instead, we propose how to use stable and radioactive carbon isotopes together to determine the sources of carbon. Our study aims to guide future work and help understand how carbonate buffering impacts CO_2 patterns across stream environments.

1. Introduction

Rivers and streams are increasingly recognized as integral components of the terrestrial carbon cycle (Cole et al., 2007; Drake et al., 2018; Raymond et al., 2013), through which carbon dioxide (CO_2) produced both in the terrestrial subsurface and stream corridor (including surface waters and hyporheic zone) environments are released into the atmosphere (e.g., Hotchkiss et al., 2015). Current estimates suggest global CO_2 emissions from inland waters are roughly half as large as anthropogenic emissions and comparable the net terrestrial carbon sink (DelSontro et al., 2018; Friedlingstein et al., 2022; Gómez-Gener et al., 2021; Lauerwald et al., 2023; Raymond et al., 2013; Sawakuchi et al., 2017); thus, the ability to quantify the magnitude and variability of these fluxes is necessary for gauging terrestrial climate feedbacks. Despite their importance in the terrestrial carbon cycle, the relative balance of CO_2 sources that support carbon fluxes to the atmosphere, which include groundwater sources such as soil respiration and subsurface chemical weathering reactions, or stream corridor sources

Writing – review & editing: Matthew J. Winnick, Brian Saccardi

including respiration of organic matter within the hyporheic zone and water-column as balanced by photosynthesis, remains uncertain. More recently, studies have shown the potential role of carbonate buffering reactions to contribute to evasing fluxes and spatial patterns of stream CO_2 partial pressure (pCO_2) (Duvert et al., 2019; Kirk & Cohen, 2023; Stets et al., 2017; Wang et al., 2021). Crucially, these buffering dynamics are not typically included in freshwater system carbon budgets and may represent an overlooked aspect of terrestrial-aquatic carbon cycling.

Carbonate buffering reactions are historically well-described within the ocean carbon literature (Broecker et al., 1979; Revelle & Suess, 1957); however, relatively few studies have investigated these dynamics in terrestrial water systems where alkalinity and dissolved CO_2 concentrations vary by orders of magnitude. Briefly, dissolved CO_2 is subject to the reaction,

$$CO_{2(aq)} + H_2O \leftrightarrow H^+ + HCO_3^-. \tag{1}$$

This reaction on its own does not alter alkalinity, and essentially acts to "store" dissolved CO_2 at levels above what would be predicted using gas solubility alone. Conceptually, the role of this CO_2 "storage" can be demonstrated through the application of Le Chatelier's principle, by which a reaction will occur to partially negate any changes to a system: (a) as dissolved CO_2 concentrations increase, for example, as rainfall equilibrates with elevated pCO_2 in the soil environment during infiltration, this causes Equation 1 to move from left to right, "storing" CO_2 in the form of $HCO_3^- + H^+$; (b) when CO_2 concentrations decrease, for example, as groundwater exits the subsurface at a seep and begins to equilibrate with the atmosphere, Equation 1 moves from right to left, acting to replenish dissolved CO_2 concentrations as degassing proceeds. Importantly, the amount of CO_2 that can be "stored" in this manner increases with increasing alkalinity (Broecker et al., 1979; Revelle & Suess, 1957). Notably, these carbonate buffering reactions may involve CO_2 of both terrestrial and aquatic origins.

These storage dynamics have been shown to operate within stream systems, and particularly in those with high alkalinity. In a compilation of US stream data, Stets et al. (2017) showed that diurnal changes in dissolved CO_2 reflecting stream metabolism are smaller than diurnal DIC changes, and that this difference increases with higher stream alkalinity. This effect leads to temporal hysteresis in CO_2:O_2 ratios as DIC concentrations take longer to adjust than O_2 to changing metabolic rates. Further, Stets et al. (2017) suggest that this effect is responsible for the observations of high downstream pCO_2 in high alkalinity streams despite significant degassing during downstream transport. These buffering reactions may also contribute significantly to total stream emissions (e.g., Kirk & Cohen, 2023); for example, Duvert et al. (2019) found that up to 60% of emissions were supported by carbonate buffering at some locations within a high alkalinity, tropical Australian river system.

Carbonate buffering dynamics also impact the evolution of carbon isotopes in DIC (e.g., Venkiteswaran et al., 2014), both in terms of stable carbon ratios ($\delta^{13}C$) and radiocarbon ratios ($\Delta^{14}C$); however, these effects have not been explored in detail within stream systems. Stable carbon isotopes are frequently used to partition DIC sources, as respired organic carbon, DIC from carbonate mineral weathering, and atmospheric CO_2 have distinct isotope compositions (e.g., Campeau et al., 2017, 2018; Polsenaere & Abril, 2012). Further, the evolution of $\delta^{13}C$ values along stream reaches may provide information on degassing rates as ^{12}C is preferentially lost to the atmosphere, reflecting both kinetic fractionation of diffusion and equilibration with atmospheric CO_2, which often has a higher $\delta^{13}C_{CO_2}$ value than stream waters. Measured $\Delta^{14}C_{DIC}$ values may also be used to partition DIC sources based on their age characteristics (Cole et al., 2022; Sveinbjörnsdóttir et al., 2020). For example, respiration of modern organic matter represents near-atmospheric $\Delta^{14}C$ values, whereas the respiration of geogenic organic carbon and weathering of carbonate rock result in low $\Delta^{14}C$ values. Previous work has shown that the radiocarbon composition of DIC equilibrates more slowly than CO_2, with apparent ^{14}C gas exchange velocities roughly 5–500x lower than typical CO_2 velocities, which has been attributed to carbonate buffering dynamics (Bourke et al., 2014). However, the quantitative impacts of carbonate buffering on $\Delta^{14}C$ equilibration has not been previously investigated to our knowledge.

Here, we develop a parsimonious model to investigate how carbonate buffering reactions impact atmospheric equilibration of river and stream DIC pools in terms of overall CO_2 fluxes and equilibration timescales. While this investigation is model-based, the thermodynamic principles that underlie these equations have been long-established. Rather than a direct model-observation comparison, these model experiments are used to develop a generalizable framework to better conceptualize the role of carbonate buffering in terrestrial-aquatic carbon cycling and guide sampling strategies and data interpretation schemes across a broad range of environments. The goals of this study are to quantify the impacts of alkalinity on (a) stream CO_2 concentration patterns and fluxes; and (b) the isotopic composition of DIC, including stable and radiogenic isotopes, and isotopic methods for partitioning stream DIC sources.

2. Methods

2.1. Carbonate System Geochemistry

To model the speciation of DIC in terrestrial streams and rivers, we incorporate reactions representing the dissolution of CO_2 gas in water, the dissociation of $CO_{2(aq)}$ (defined here as equivalent carbonic acid, $H_2CO_{3(aq)}$), and the dissociation of the bicarbonate as applied separately to ^{12}C, ^{13}C, and ^{14}C DIC species. These reactions and their associated equilibrium constants at 25°C are shown in Table 1, and are based on the methodology of Druhan et al. (2021). Briefly, for a given reaction x, the ratio of equilibrium constants (K_x) for DIC isotopologues sets the equilibrium fractionation factor as,

$$\alpha_x = \frac{K_x^i}{K_x^{12}}, \tag{2}$$

where i represents either ^{13}C or ^{14}C versions of reaction x. We use the equilibrium constants of Druhan et al. (2021) for ^{13}C and ^{14}C, assuming that fractionation factors are doubled for ^{14}C relative to ^{13}C based on their relative mass differences with ^{12}C.

2.2. Evolution of the Carbonate System During Degassing

To model the evolution of stream DIC concentrations and isotopic composition during degassing, we simulate three distinct scenarios of increasing complexity:

- Scenario 1: Groundwater seep degassing with no additional CO_2 inputs
- Scenario 2: Groundwater seep degassing with continuous inputs of CO_2 from groundwater and stream corridor respiration
- Scenario 3: An 87 km^2 watershed river network in Gothic, CO for which we have previously developed and validated a reactive transport model incorporating groundwater inputs, water-column net respiration and hyporheic zone CO_2 sources (Saccardi & Winnick, 2021).

These scenarios and the processes incorporated into each are diagrammed conceptually in Figure 1.

2.2.1. Scenario 1: Groundwater Seep Degassing With No Additional Carbon Sources

In Scenario 1, we model a groundwater parcel degassing during stream transport with no additional carbon sources during transport (Figure 1a). This would correspond physically to a spring seep with no additional along-stream groundwater inputs or net respiration. In this scenario, the changes in DIC concentrations are modeled as,

$$\frac{\partial \mathrm{DIC}}{\partial t} = -K_{CO_2}\left(CO_{2(aq)} - CO_{2(aq)sat}\right), \tag{3}$$

where K_{CO_2} is the reaeration coefficient of CO_2, $CO_{2(aq)}$ is the dissolved CO_2 concentration, and $CO_{2(aq)sat}$ is the theoretical concentration of CO_2 in equilibrium with an atmospheric pCO_2 of 410 ppm.

We assume an initial DIC value of groundwater (DIC_{gw}) based on a specified groundwater pCO_2 (20,000 ppm) (Jungkunst et al., 2008; Kessler & Harvey, 2001) and alkalinity, which ranges in our experiments from 0 to 6 meq/L based on the range of freshwater stream alkalinity values from a compilation of United States surface waters (Stets et al., 2017). The resulting DIC_{GW} was calculated as 0.179–6.15 mM depending on alkalinity using a temperature

Table 1
Reaction Network and End-Member Source Values for Modeling Experiments

Reaction	$\log(K^{12})$ @ 25°C	$\log(K^{13})$ @ 25°C	$\log(K^{14})$ @ 25°C
Reaction Network			
$^iCO_{2(aq)} \leftrightarrow H^+ + H^iCO_3^-$	−6.3447	−6.340835	−6.336995
$H^iCO_3^- \leftrightarrow H^+ + {}^iCO_3^{2-}$	−10.3288	−10.328986	−10.32914
$H_2O \longleftrightarrow H^+ + OH^-$	−14[a]	–	–
Source	pCO_2 (ppm)	$\delta^{13}C$ (‰ VPDB)	$\Delta^{14}C$ (‰)
End-member Sources			
Groundwater	20,000	−15	−500
Stream Corridor Respiration	–	−27	−66
Atmosphere	410	−9	−66

[a] log(K).

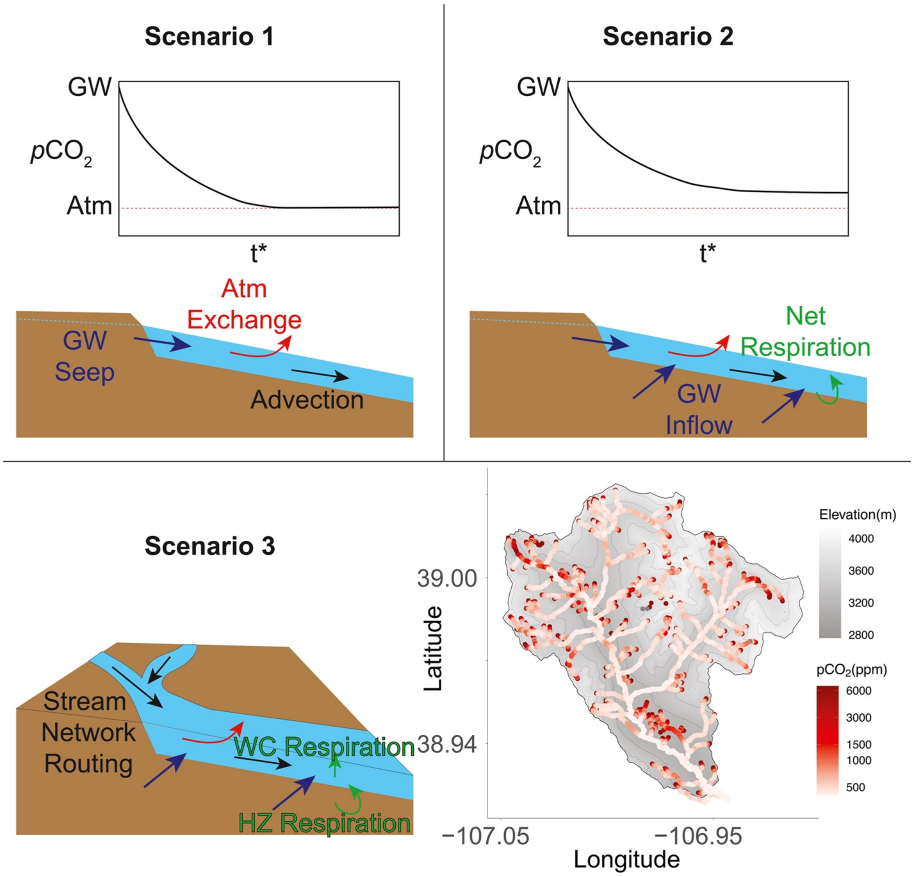

Figure 1. Conceptual diagram of the modeling scenarios including characteristic patterns of pCO_2 and the incorporated processes. Scenario 1 is analogous to a degassing groundwater seep with no additional CO_2 inputs. Scenario 2 represents a groundwater seep degassing with simultaneous CO_2 inputs from groundwater and stream corridor respiration, analogous to a small headwater stream. Scenario 3 is the modeling of a full 87 km^2 5th order watershed in the East River, CO, USA. It incorporates stream network water routing via advection, groundwater inputs, hyporheic exchange, net water column respiration, and atmospheric exchange. Simulated watershed pCO_2 values are from Saccardi and Winnick (2021) and represent a no-alkalinity simulation, which is compared to the updated model in Scenario 3. Note that symbol definitions translate between Scenarios, and groundwater Seep and Inflow end-member values are identical.

of 25°C. We additionally specify a K_{CO_2} value (0.0002 s^{-1}); however, our analysis examines CO_2 evolution over non-dimensional timescale (t^*) calculated as $t^* = (t)\,(K_{CO_2})$ (unitless); thus, the results are scalable to any given K_{CO_2} value. The model is then solved using an explicit numerical approximation over discretized timesteps. At each timestep following the calculation of a new DIC value, the carbonate system is speciated using alkalinity and the updated DIC concentration, following the methods of Venkiteswaran et al. (2014). Briefly, we develop a system of equations based on the equilibrium constants in Table 1, along with equations for alkalinity (Alk) and DIC as,

$$\text{Alk} = \left[\text{HCO}_3^-\right] + 2\left[\text{CO}_3^{2-}\right] + \left[\text{OH}^-\right] - \left[\text{H}^+\right] \tag{4}$$

and

$$\text{DIC} = \left[\text{CO}_{2(aq)}\right] + \left[\text{HCO}_3^-\right] + \left[\text{CO}_3^{2-}\right], \tag{5}$$

respectively.

Model calculation scripts using R software are included in Supporting Information S1.

We solve Equation 3 and speciate the DIC pool separately for each isotopologue of carbon. For simplicity, we assume that the reaeration coefficients are the same for ${}^{12}CO_2$, ${}^{13}CO_2$, and ${}^{14}CO_2$. While degassing experiments suggest mass-dependent kinetic fractionation of ∼0.998 for $^{13}CO_2/^{12}CO_2$ (e.g., Zhang et al., 1995), fractionation associated with turbulent atmospheric exchange, which dominates in most river systems, has not been adequately characterized. We note that our equations are flexible to incorporate kinetic fractionation as,

$$\alpha_k = \frac{k^i}{k^{12}}, \tag{6}$$

where i denotes the reaeration coefficient k for either $^{13}CO_2$ or $^{14}CO_2$, following the formulation of Zhang et al. (1995), though for the purposes of our model experiments, we assume $\alpha_k = 1$. We also note that within our model simulations, ^{12}C degasses faster than ^{13}C due to a larger proportional offset between atmospheric and stream $^{12}CO_2$ concentrations. This causes apparent fractionation as the stream equilibrates with atmospheric boundary conditions; however, it does not physically represent kinetic fractionation. We note that these two processes that cause increasing $\delta^{13}C$ values during degassing are not often discussed as separate processes and are typically referred to collectively as fractionation during degassing.

We calculate $\delta^{13}C$ and $\Delta^{14}C$ values as,

$$\delta^{13}C = \left(\frac{R_{\text{sample}}}{R_{\text{std}}} - 1\right) * 1000‰, \tag{7}$$

and

$$\Delta^{14}C = \left(\frac{\left({}^{14}C/{}^{12}C\right)_{\text{corr}}}{\left({}^{14}C/{}^{12}C\right)_{\text{std}} * \exp\left(\frac{2023-1950}{8267}\right)} - 1\right) * 1000‰, \tag{8}$$

where

$$\left({}^{14}C/{}^{12}C\right)_{\text{corr}} = \left({}^{14}C/{}^{12}C\right)_{\text{sample}}\left(\frac{1+\delta^{13}C_{\text{std}}/1000}{1+\delta^{13}C_{\text{sample}}/1000}\right)^2. \tag{9}$$

Within these equations, R_{std} represents the $^{13}C/^{12}C$ ratio of the VPDB standard, and $^{14}C/^{12}C_{\text{std}}$ is 1.12E–12. Equation 9 essentially corrects for equilibrium fractionation effects within the ^{14}C system. In this scenario and across the following sections, we assume an initial groundwater $\delta^{13}C_{DIC}$ value of −15‰ representing a balance of C_3 soil respiration and carbonate from calcite weathering (Campeau et al., 2017) and $\Delta^{14}C_{DIC}$ value of −500‰ representing a mix of modern soil respiration and ^{14}C-dead carbonate carbon based on the stoichiometry of calcite dissolution ($CaCO_{3(s)} + H_2CO_{3(aq)} \rightarrow Ca^{2+} + 2HCO_3$; Table 1). We also assume that on the timescales of stream transport, radioactive decay of ^{14}C is negligible.

2.2.2. Scenario 2: Continuous Groundwater and Stream Corridor CO_2 Sources

In Scenario 2, we incorporate continuous inputs from groundwater inflows and stream corridor CO_2 production via aerobic respiration (Figure 1b). In this scenario, we amend Equation 3 to incorporate these inputs as,

$$\frac{\partial \text{DIC}}{\partial t} = -k\left(CO_{2(aq)} - CO_{2(aq)sat}\right) + Q\left(\text{DIC}_{gw} - \text{DIC}\right) + F_{\text{prod}}, \tag{10}$$

where Q is the volume-normalized groundwater inflow rate (s^{-1}), and F_{prod} is the net respiration (mol/L/s) within both the water column and the hyporheic zone, which we define as stream corridor respiration here, though we split this term into the individual contributions from net water column respiration and hyporheic zone respiration in Scenario 3. This method assumes that alkalinity remains constant, ignoring potential variability in groundwater inflow alkalinities, anaerobic respiration that may contribute additional alkalinity, and carbonate precipitation which would decrease alkalinity. This situation is analogous to a homogenous stream reach with active groundwater inputs. Similar to Scenario 1, we solve this equation using an explicit numerical scheme across discretized timesteps. The same methods are applied, whereby at each timestep, a new DIC value is calculated and the DIC system is speciated based on the Venkiteswaran et al. (2014) scheme. As above, groundwater is specified with a pCO_2 of 20,000 ppm; $\delta^{13}C_{DIC}$ value of −15‰ representing a balance of C_3 soil respiration and carbonate from calcite weathering; and $\Delta^{14}C_{DIC}$ of −500‰ representing a mix of modern soil respiration and ^{14}C-dead carbonate carbon. Stream corridor respiration is assumed to have a $\delta^{13}C_{DIC}$ value of −27‰ and $\Delta^{14}C_{DIC}$ of −66‰ representing modern carbon. As in Scenario 1, we vary alkalinity across our simulations from 0 to 6 meq/L though for simplicity we include only 0.1, 1.0, and 4.0 meq/L simulations in the main text. We also vary input flux rates as 10^{-7} (low), 10^{-6} (med), and $10^{-5.5}$ (high) mol/L/s (Izagirre et al., 2008) and the ratio of input fluxes from groundwater versus stream corridor respiration with ratio values of 0.001 (99.9% groundwater), 1 (equal contributions), and 1,000 (99.9% stream corridor respiration).

2.2.3. Scenario 3: Stream Network CO_2 Model

Finally, to explore the complexity of alkalinity controls on stream network-scale CO_2 and isotope dynamics, we incorporate DIC speciation reactions into an existing stream network advection-reaction model of dissolved CO_2 (Figure 1). This model was originally developed, applied, and validated for the East River watershed in Gothic, CO, USA (Saccardi & Winnick, 2021). Briefly, the East River watershed is an 87 km^2, high elevation, mountainous watershed, with annual flow dominated by spring snowmelt (Winnick et al., 2017). In this model, we consider CO_2 fluxes from (a) groundwater with a specified pCO_2 and inflow fluxes that scale with changes in upstream accumulating area and specified runoff values reflecting flow conditions from August 2019; (b) hyporheic exchange parameterized using a surface renewal-theory mass-transfer model (Grant et al., 2018; Winnick, 2021) and assuming a constant offset between hyporheic zone and stream CO_2 meant to reflect net respiration; (c) water column net respiration at a specified volume-normalized rate; and (d) atmospheric exchange in which gas exchange velocities (k_{600}) are parameterized based on slope and discharge via empirical correlations between energy dissipation rates and k_{600} (Ulseth et al., 2019). The full details of model derivation and parameterization are presented in Saccardi and Winnick (2021), and the simulated map of stream pCO_2 values is shown in Figure 1. Here, we update the model and simplify a number of model parameterizations as (a) we ignore wetland contributions and assume all groundwater sources have the same pCO_2 across the watershed, as opposed to our original model which specified high pCO_2 values from wetland areas; (b) we ignore snow-plugs which were introduced into the model as zones with no atmospheric gas exchange to match field observations. For simplification, we assume a single groundwater alkalinity value for the whole watershed, and that stream-corridor respiration does not alter alkalinity, ignoring, for example, alkalinity contributions from anaerobic respiration. Finally, we update the underlying model equations to incorporate DIC speciation as,

$$\frac{\partial \mathrm{DIC}}{\partial t} = -v\frac{\partial \mathrm{DIC}}{\partial x} - k\left(\mathrm{CO}_{2(\mathrm{aq})} - \mathrm{CO}_{2(\mathrm{aq})\mathrm{sat}}\right) + Q\left(\mathrm{DIC}_{\mathrm{gw}} - \mathrm{DIC}\right) + F_{\mathrm{wc}} + k_{\mathrm{hz}} * C_{\mathrm{hz}}, \tag{11}$$

where v is advection velocity (m/s), x is distance along a stream (m), F_{wc} is the water column net respiration flux (ER—GPP; mol/L/s), k_{hz} is the rate of hyporheic exchange (s^{-1}), and C_{hz} is the offset between stream and hyporheic zone DIC (mol/L). In relation to the previous scenario, we have here split net stream corridor respiration (F_{prod}) into explicit water column (F_{wc}) and hyporheic zone ($k_{hz}*C_{hz}$) components. This model is applied to NHD HR streamlines at sub-reach scales. In this model exercise, we assume steady-state conditions (e.g. $\partial \mathrm{DIC}/\partial t = 0$), and use a backwards-difference method to solve for changes in DIC spatially across the stream network. At each new downstream spatial grid, we then use the updated DIC and the specified alkalinity value to speciate the DIC system. For modeled cells, we discretized NHD HR stream flowlines at a 0.5 m spacing.

We solve the model separately for three alkalinity values: 0.1, 1 (roughly the average measured site alkalinity), and 4 meq/L. We assume groundwater pCO_2 of 20,000 ppm in the range of measured soil values (Winnick et al., 2020), an elevation of hyporheic zone pCO_2 above stream values of 700 ppm, and an F_{wc} value of 10^{-9} mol/L/s, roughly aligning with optimized values from the model validation of Saccardi and Winnick (2021). Crucially, our intent here is not to validate the model against previous field observations, but instead to interrogate how the carbonate buffering dynamics explored the idealized Scenario's 1 and 2 may be reflected in real-world systems. Given the previous studies which have shown the importance of carbonate weathering for generating alkalinity within the East River system (Carroll et al., 2018; Winnick et al., 2017), we assume end-member isotope compositions from Scenario 2, shown in Table 1.

3. Results

3.1. Scenario 1 Results

The temporal evolution of pCO_2, $\delta^{13}C_{DIC}$, and $\Delta^{14}C_{DIC}$ for our groundwater degassing simulations (scenario 1) are shown in Figure 2 across a range of alkalinities. Within these plots, the time axis (t*) is non-dimensional,

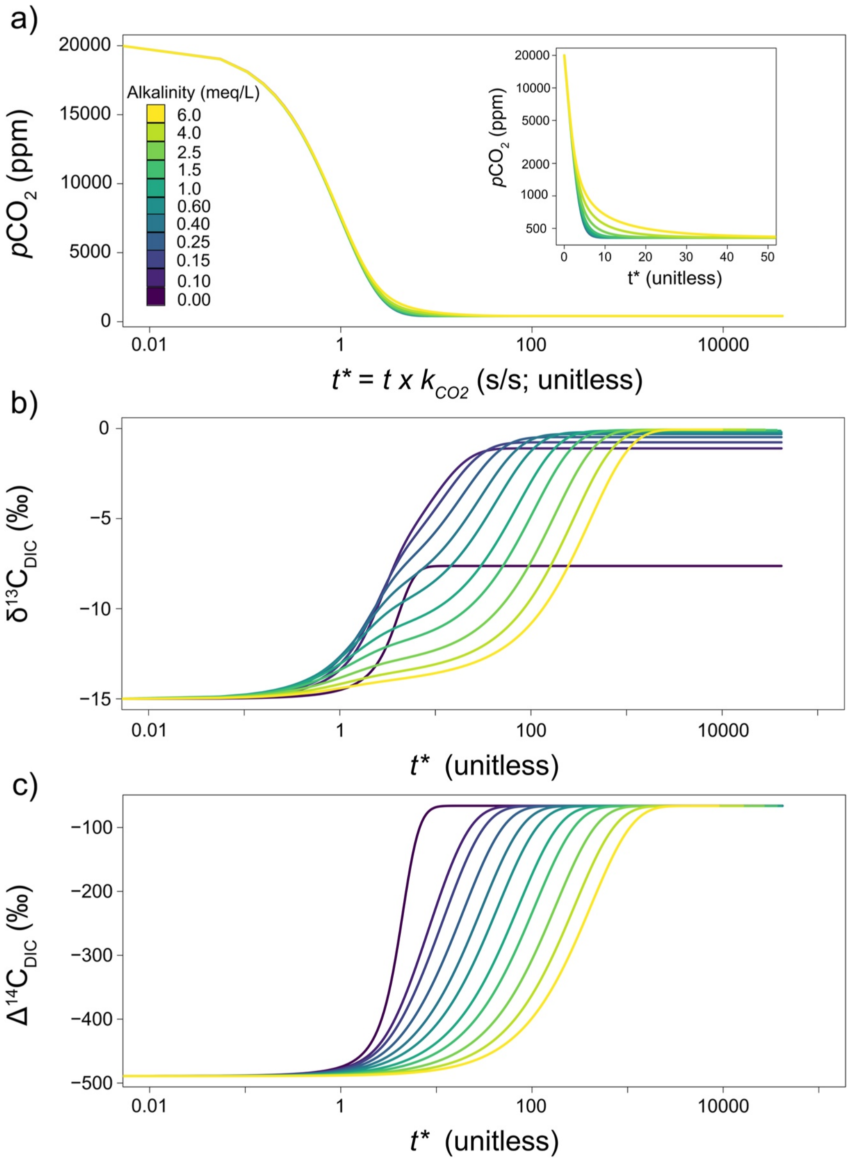

Figure 2. Temporal evolution of (a) pCO_2, (b) $\delta^{13}C_{DIC}$, and (c) $\Delta^{14}C_{DIC}$ in Scenario 1 simulations. The x-axis in all plots represents nondimensional time, calculated by multiplying simulation time (s) at the specified reaeration rate (s^{-1}). Line colors represent the specified groundwater alkalinity. Note that the large difference between the 0 and 0.1 meq/L alkalinity lines in plot (b) reflects the non-linear decrease in the fractional contribution of $CO_{2(aq)}$ to total DIC as alkalinity increases.

representing the simulation time (s) multiplied by the specified reaeration rate (s^{-1}); these values are also equivalent to non-dimensional distance, and simulation time could be scaled to a dimensional distance by multiplying by an advective velocity. As shown in the top panel, high initial groundwater pCO_2 values equilibrate with atmospheric values over t^* timescales of ~5–40 (unitless). Higher alkalinity values result in slightly longer pCO_2 equilibration timescales, as highlighted by the inset in Figure 2a, though values eventually approach the same atmospheric pCO_2 levels. This increase in the equilibration timescale is controlled by carbonate buffering reactions, which act to resupply CO_2 as degassing progresses, as discussed in the Introduction (Equation 1). These changes in equilibration timescales due to carbonate buffering are relatively muted as compared to isotopic equilibration, which we discuss below.

In Figure 2b, $\delta^{13}C_{DIC}$ starts at groundwater values of −15‰ and approaches equilibrium with atmospheric $\delta^{13}C_{CO_2}$ values of −9‰ through time. Importantly, the final equilibrated $\delta^{13}C_{DIC}$ values vary as a function of alkalinity. Under zero alkalinity conditions, equilibrated $\delta^{13}C_{DIC}$ is slightly elevated (−7.6‰) above atmospheric values as

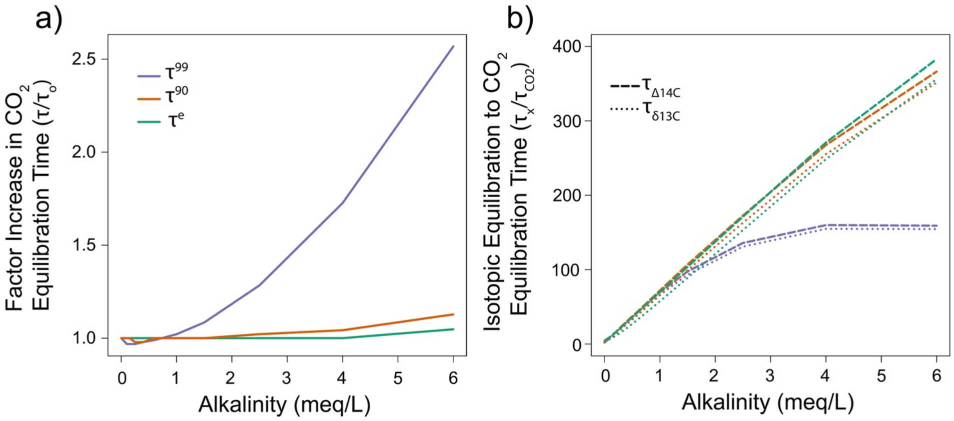

Figure 3. Impacts of alkalinity on atmosphere equilibration timescales for Scenario 1 simulations of (a) pCO_2, and (b) $\delta^{13}C_{DIC}$ and $\Delta^{14}C_{DIC}$ relative to pCO_2. Line colors represent different metrics of equilibration timescales. Dashed and dotted lines in (b) represent $\Delta^{14}C_{DIC}$ and $\delta^{13}C_{DIC}$, respectively.

CO_2 is only ~84% of total DIC. As alkalinity increases, CO_2 quickly becomes a secondary component of DIC at atmosphere equilibration; for example, CO_2 is only 12% of total atmosphere-equilibrated DIC at an alkalinity of 0.1 meq/L. As alkalinity increases, equilibrated $\delta^{13}C_{DIC}$ values approach HCO_3^- and CO_3^{2-} values, which due to equilibrium fractionation are elevated ~9‰ above $CO_{2(aq)}$ values. Thus, the DIC pool approaches ~0‰ when equilibrated with the atmosphere. In addition to these changes in the final equilibrated values, alkalinity also strongly impacts the timescales of equilibration. Under zero alkalinity conditions, isotopic equilibration timescales are comparable to those of pCO_2. As alkalinity increases, however, $\delta^{13}C_{DIC}$ equilibration timescales increase significantly, with the high alkalinity (6 meq/L) scenario requiring non-dimensional timescales of >1,000 as compared to CO_2 equilibration timescales of ~50.

Values of $\Delta^{14}C_{DIC}$ display similar patterns with a few important differences (Figure 2c). First, alkalinity has no impact on final $\Delta^{14}C_{DIC}$ values, as the associated equilibrium fractionation is normalized for within Equation 9. However, as equilibrium fractionation is roughly twice as large for ^{14}C as ^{13}C, a larger initial proportion of ^{14}C is buffered within the $HCO_3^- + CO_3^{2-}$ DIC pool, thus timescales of equilibration are slightly larger.

In Figure 3a, we directly evaluate these timescales of equilibration through the calculation of folding-times of $\boldsymbol{\tau}^{99}$, $\boldsymbol{\tau}^{90}$, and $\boldsymbol{\tau}^{e}$ representing the non-dimensional time required to degas 99%, 90%, and ~36% of groundwater CO_2, respectively. Figure 3a shows the factor increase in each of these timescales for a range of alkalinities compared to a simulation with no alkalinity. Alkalinity has relatively little impact on the $\boldsymbol{\tau}^{90}$ and $\boldsymbol{\tau}^{e}$ timescales, though it causes an increase of over 2.5x in $\boldsymbol{\tau}^{99}$ in the high alkalinity simulation. Given the nature of our non-dimensional analysis, this factor increase is a scalable result. In other words, for any given combination of reaeration rates, stream velocities, and initial pCO_2 values, this would result in a 2.5x increase in the distance over which a groundwater seep degassed 99% of its CO_2. Physically, this sensitivity of $\boldsymbol{\tau}^{99}$ values demonstrates that the impact of carbonate buffering is highest at near-atmospheric pCO_2, resulting in longer timescales to lose the final 1% of pCO_2, and is visually evident in Figure 2a as the alkalinity curves diverge only as they approach atmospheric values.

The ratio of isotopic equilibration timescales to pCO_2 equilibration is shown in Figure 3b. Increases in alkalinity result in roughly linear increases in the ratio of these equilibration timescales for $\boldsymbol{\tau}^{90}$ and $\boldsymbol{\tau}^{e}$. In contrast, $\boldsymbol{\tau}^{99}$ values plateau above an alkalinity of ~4 meq/L and diverge from $\boldsymbol{\tau}^{90}$ and $\boldsymbol{\tau}^{e}$ at ~1.5 meq/L alkalinity. Importantly, the impacts on equilibration timescales are very similar between $\delta^{13}C_{DIC}$ and $\Delta^{14}C_{DIC}$, to small variations due to differing equilibrium fractionation factors that result in slight differences in the proportion of ^{13}C versus ^{14}C buffered by the HCO_3^- and CO_3^{2-} pools.

Lastly, for Scenario 1, we calculate the proportion of CO_2 emissions supported by carbonate buffering across a range of alkalinity and groundwater pCO_2 values, as shown in Figure 4. This value is calculated by subtracting the total loss of $CO_{2(aq)}$ during atmospheric equilibration from the total DIC loss during equilibration, normalized by the total DIC loss. Carbonate buffering plays a negligible role in CO_2 emissions when alkalinity is low and groundwater pCO_2 is high, as both of these conditions result in smaller proportional storage of CO_2

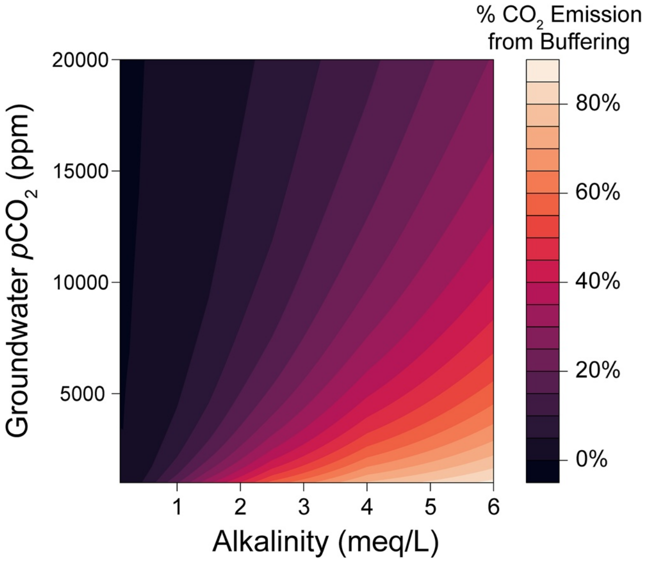

Figure 4. Contour map of the % contributions of carbonate buffering reactions to total CO_2 emissions in Scenario 1 as a function of groundwater alkalinity and pCO_2. Carbonate buffering reactions contribute proportionally more to overall emissions as groundwater alkalinity increases and groundwater pCO_2 decreases.

as $HCO_3^- + H^+$. However, under conditions of high alkalinity and low groundwater pCO_2, carbonate buffering may account for up to 90% of emissions. While carbonate buffering dominates emissions, we note that the total amount of CO_2 degassed is low compared with high groundwater pCO_2—low alkalinity conditions. We note that these estimates assume no calcite precipitation. This may become an important factor in high alkalinity systems with available Ca^{2+}, whereby degassing raises the calcite saturation state leading to mineral precipitation and further buffering of $CO_{2(aq)}$ concentrations.

3.2. Scenario 2 Results

In Scenario 2, we incorporate continuous groundwater and net stream corridor respiration fluxes during seep degassing, reflecting more realistic scenarios in which evasion fluxes are partially supported by localized CO_2 sources. The temporal patterns of pCO_2, $\delta^{13}C_{DIC}$, and $\Delta^{14}C_{DIC}$ are shown in Figure 5 across a range of alkalinities, total CO_2 source fluxes, and ratios of groundwater to stream corridor sources. Across Figures 5a–5c, pCO_2 displays patterns similar to Figure 2. As total CO_2 sources increase, steady-state pCO_2 values increase to well above atmosphere-equilibrated values. These elevated pCO_2 values represent a stable balance between specific input fluxes and evasion rates, which can be calculated by assuming steady-state ($dC/dt = 0$) and rearranging Equation 10 as,

$$CO_{2(aq)steady-state} = \frac{Q\left(DIC_{gw} - DIC\right) + F_{prod}}{k} + CO_{2(aq)sat}. \tag{12}$$

As steady-state pCO_2 values increase, the effects of alkalinity on degassing patterns become more muted. For example, in Figure 5c, there is little visible difference between the high alkalinity simulation (4 meq/L) and the low alkalinity simulation (0.1 meq/L). This demonstrates similar patterns as in Figure 3a, which shows that the impacts of equilibration timescales are relatively insignificant when evaluated at pCO_2 levels above atmospheric (i.e., $\boldsymbol{\tau}^{90}$ and $\boldsymbol{\tau}^{e}$). Patterns of pCO_2 are not impacted by the partitioning of fluxes between groundwater and stream corridor sources, assuming that the total fluxes are the same.

Carbon isotope patterns become more complicated when considering multiple sources of different compositions. This is most clear for $\delta^{13}C_{DIC}$ where atmospheric, groundwater, and stream corridor respiration all have different sources, versus $\Delta^{14}C_{DIC}$ where stream corridor and atmospheric sources are roughly the same. Broadly, increased alkalinity results in increasing steady-state timescales for both $\delta^{13}C_{DIC}$ and $\Delta^{14}C_{DIC}$, with timescales of ~1 for no alkalinity to >100 for high alkalinity scenarios. These steady-state timescales are not significantly impacted by the magnitude of CO_2 source fluxes or their partitioning between groundwater and stream corridor respiration (i.e., comparing the yellow lines within and across the panels). Alkalinity also impacts the final steady-state value of $\delta^{13}C_{DIC}$ for a given CO_2 source flux and partitioning ratio (i.e., comparing the solid purple curve to the solid yellow curve within a panel), such that low alkalinity results in a lower $\delta^{13}C_{DIC}$ value for a given flux and partitioning ratio of carbon inputs.

Across these simulations, steady-state $\delta^{13}C_{DIC}$ and $\Delta^{14}C_{DIC}$ are also highly sensitive to both the magnitude of total source fluxes and their partitioning between groundwater and stream corridor sources. In the case of $\delta^{13}C_{DIC}$, as both groundwater and stream corridor sources have lower-than-atmospheric values, increasing CO_2 input flux results in a decrease in steady-state values. Further, as $\delta^{13}C_{DIC}$ of stream corridor sources are lower than groundwater (−27‰ vs. −15‰ in these simulations), a higher proportion of stream corridor source results in lower steady-state $\delta^{13}C_{DIC}$ values. Comparing across Figures 5d–5f, we note a significant degree of equifinality in steady-state $\delta^{13}C_{DIC}$ values, whereby different combinations of alkalinity, total CO_2 sources, and source partitioning can result in similar steady-state $\delta^{13}C_{DIC}$ values. Even if alkalinity is constrained, different combinations of CO_2 sources with different $\delta^{13}C_{DIC}$ end-member values can result in the same steady-state $\delta^{13}C_{DIC}$. For example, a low alkalinity stream with medium CO_2 inputs coming from stream corridor respiration (green solid line, Figure 5e) features similar steady-state $\delta^{13}C_{DIC}$ as a low alkalinity stream with high CO_2 inputs coming equally from groundwater and stream corridor respiration (green dashed line, Figure 5f).

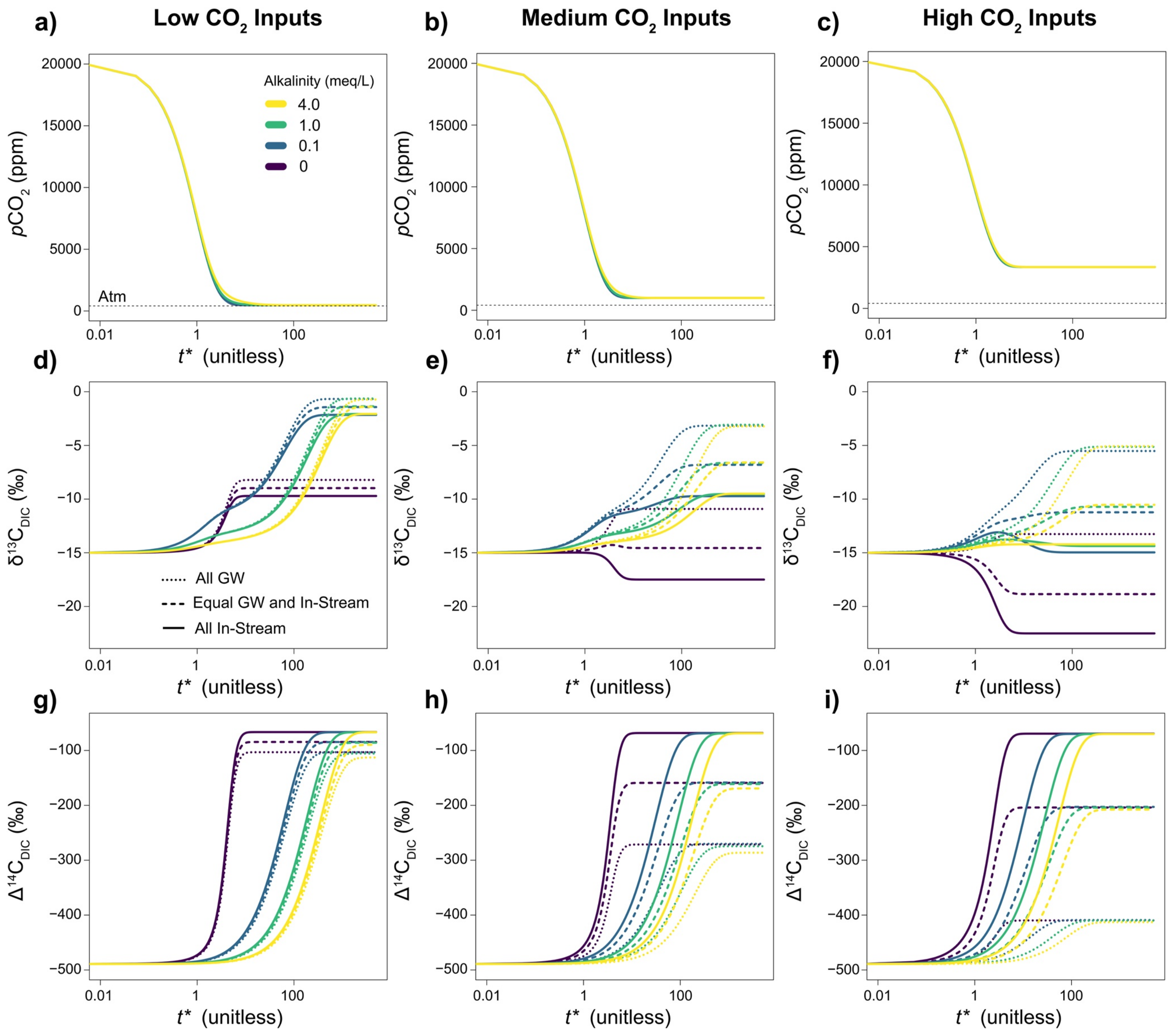

Figure 5. Temporal evolution of simulations in Scenario 2 showing pCO$_2$, δ^{13}C$_{\text{DIC}}$, and Δ^{14}C$_{\text{DIC}}$ (rows) for varying CO$_2$ input fluxes (columns). *X*-axes represent non-dimensional time. The line color represents alkalinity, and line types represent the ratio of groundwater versus stream corridor respiration contributions to CO$_2$ inputs.

The controls of sources on steady-state values are more easily discernible in the Δ^{14}C$_{\text{DIC}}$ data, where values are not sensitive to alkalinity. As we set Δ^{14}C$_{\text{DIC}}$ values of stream corridor respiration to near-atmospheric, stream corridor respiration does not have a significant impact on Δ^{14}C$_{\text{DIC}}$ steady-state values (i.e., comparing the solid lines across panels g–i). Instead, variability is controlled by the total magnitude of groundwater CO$_2$ fluxes, which act as a source of low Δ^{14}C$_{\text{DIC}}$ and draw down steady-state values.

3.3. Scenario 3 Results

In this exercise, we compare the results of those simulations, which only represented the CO$_2$ component of the DIC system (equivalent to a situation with an alkalinity of 0), with our updated model. Spatial patterns of CO$_2$ are shown in Supporting Information S1 (Figures S1, S3, and S4) and do not result in significant visual differences in spatial patterns across the watershed, as depicted in the inset of Figure 1c. In contrast to our degassing experiments in Scenarios 1 and 2 in which pCO$_2$ is always decreasing to approach atmospheric concentrations,

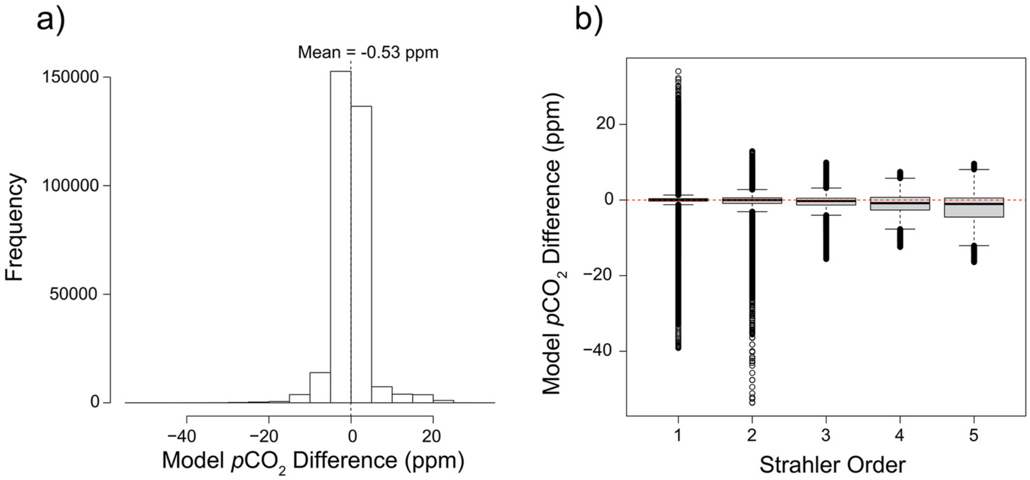

Figure 6. Comparisons of Scenario 3 simulations with 1 meq/L alkalinity and no alkalinity, showing (a) a histogram of the differences, and (b) a boxplot of differences binned by Strahler Order. The inclusion of alkalinity results in both increased and decreased simulated pCO_2, with decreased values occurring in areas with low gas exchange rates that allow for pCO_2 to build up locally. Alkalinity does not result in increased downstream pCO_2 at the stream network scale, as shown in (c).

the full watershed simulation features areas in which pCO_2 increases due to inputs (groundwater and stream corridor respiration) that are locally higher than evasion fluxes. Under these conditions, the inclusion of alkalinity results in lower pCO_2 estimates than simulations without alkalinity, as a proportion of the CO_2 inputs is stored as $HCO_3^- + H^+$. At the watershed scale, there are a comparable number of model cells in which the inclusion of alkalinity results in lower versus higher pCO_2 relative to no alkalinity (Figure 6a), with a difference range of −53–34 ppm in our 1 meq/L alkalinity simulation. This range increased with increasing alkalinity (Figures S2 and S5 in Supporting Information S1), but the overall pattern was unchanged.

Patterns in model differences are minimal when compared across stream scales, as defined by the Strahler Order in Figure 6b. Interestingly, the range of model differences decreases while standard deviations increase with the Strahler Order. There is also a slight trend toward lower pCO_2 predictions from the alkalinity model at larger stream scales, and this likely reflects flatter topography and lower gas exchange velocities in the higher order streams. Averaged across the watershed, the alkalinity model predicts slightly lower pCO_2 values by −0.054 ppm. Counterintuitively, total watershed evasion fluxes from the alkalinity model are slightly higher, due to outsized flux contributions from areas with high gas exchange velocities (where the alkalinity model predicts slightly higher pCO_2) on total fluxes. The difference in total watershed fluxes reflects the additional CO_2 stored as $HCO_3^- + H^+$ in exfiltrating groundwater, as both simulations are given the same groundwater pCO_2 and feature the same total stream corridor respiration fluxes.

We also show how carbonate buffering reactions impact relationships between pCO_2 and the isotopic composition of DIC in Figure 7 for the East River with an alkalinity of 1 meq/L, which expands on Figure 5 by incorporating scenarios with both increasing and decreasing pCO_2. During groundwater degassing in the headwaters, patterns resemble the degassing experiments from Scenario 1. However, in downstream reaches where pCO_2 experiences local variability in response to changing balances between input fluxes and evasion rates, the model output deviates significantly from the degassing patterns. When local sources act to increase pCO_2, the total amount of DIC added is relatively small compared to the existing pool, which introduces hysteresis; thus, $\delta^{13}C_{DIC}$ and $\Delta^{14}C_{DIC}$ are largely insensitive to changes in pCO_2. This behavior is highlighted in the insets in Figure 7, in which local changes in pCO_2 result in minimal $\delta^{13}C_{DIC}$ and $\Delta^{14}C_{DIC}$ changes, and overall patterns feature no large-scale co-variability. We note that in Figure 7a this decoupling occurs despite the fact that lower $\delta^{13}C_{DIC}$ values of stream corridor respiration relative to groundwater should act to drive steeper, more sensitive correlations between pCO_2 and $\delta^{13}C_{DIC}$. This decoupling of pCO_2 and $\delta^{13}C_{DIC}$ is similar under high alkalinity (Figure S6 in Supporting Information S1) and is also significant even in low alkalinity conditions of 0.1 meq/L (Figure S7 in Supporting Information S1). These results show that even under low alkalinity, pCO_2 and the isotopic composition of DIC are not covary systematically across the watershed scale except during initial groundwater degassing.

To demonstrate the potential use of paired $\delta^{13}C_{DIC}$ and $\Delta^{14}C_{DIC}$ in evaluating local partitioning between groundwater and stream corridor sources of DIC, we plot data from each model cell of the 1 meq/L simulation in $\delta^{13}C_{DIC}$

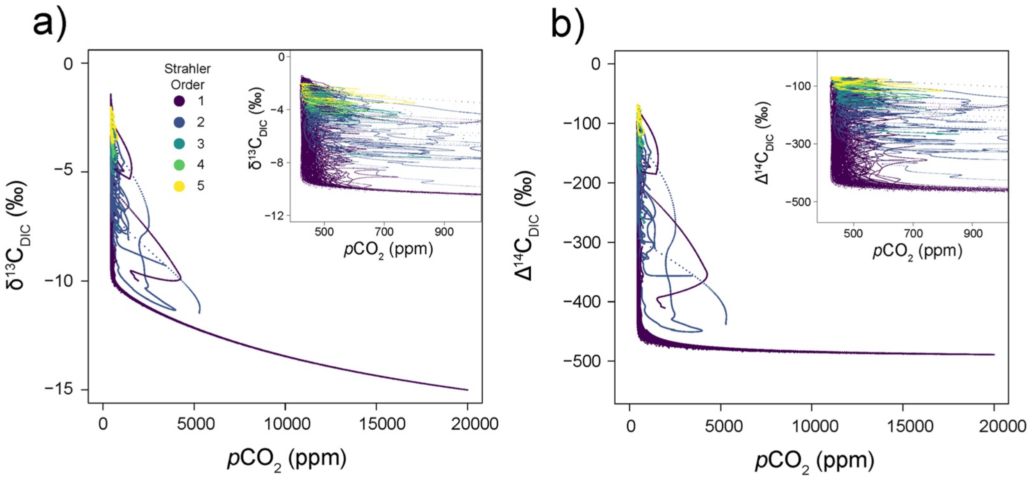

Figure 7. Simulated relationships between (a) $\delta^{13}C_{DIC}$ and pCO$_2$ and (b) $\Delta^{14}C_{DIC}$ and pCO$_2$ in the Scenario 3 simulations with 1 meq/L alkalinity. Point colors represent the Strahler Order, and the insets highlight variability following groundwater degassing. Following groundwater seep degassing in 1st order streams, pCO$_2$ and the isotopic composition of DIC are largely decoupled.

versus $\Delta^{14}C_{DIC}$ space in Figure 8a. Contour lines represent degassing patterns for an initial DIC pool representing the isotopic end-member composition of varying mixtures of groundwater and stream corridor sources, generated using the same methods as in Scenario 1. We note that while this plot resembles an end-member mixing model, there is some curvature in the contour lines that reflect slight differences in the timescales of equilibration for ^{14}C versus ^{13}C discussed above. As shown, 1st order streams largely fall along All-groundwater degassing contour lines to start with a shift toward higher contributions from stream corridor respiration as values approach atmospheric equilibration. In general, there is a trend toward higher stream corridor respiration contributions at higher stream order, with a significant degree of variability within each order. We show this directly in Figure 8b, where the % groundwater contribution to DIC is calculated using a nearest-neighbor function to find which contour line passes through each model output point. Across all model cells, groundwater contributions vary from 100%

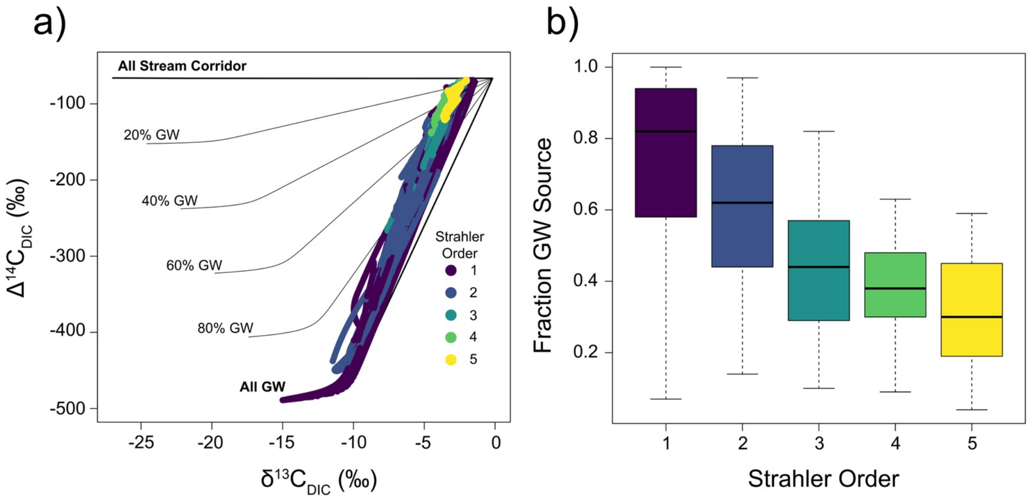

Figure 8. Carbon source partitioning using $\delta^{13}C_{DIC} - \Delta^{14}C_{DIC.}$ (a) Simulated Scenario 3 (1 meq/L alkalinity) relationships between $\delta^{13}C_{DIC}$ and $\Delta^{14}C_{DIC}$ represent contributions from stream corridor (combined water column and hyporheic zone sources), groundwater (GW), and atmospheric end-member sources. Contour lines represent degassing simulations from mixed groundwater-stream corridor end-member sources. Non-linearity of the contour curves represents slight offsets in $\delta^{13}C_{DIC}$ and $\Delta^{14}C_{DIC}$ equilibration timescales (e.g., Figure 3b). (b) Fractional contributions of DIC from groundwater sources (versus stream corridor respiration) as a function of Strahler Order. Simulations show a shift in sources from groundwater in the headwaters to stream corridor respiration in higher order streams.

to 4%. We simulate a consistent transition from groundwater to stream corridor DIC sources at larger network scales, with the switch from groundwater to stream corridor dominance occurring between 2nd and 3rd order streams, consistent with our previous modeling results (Saccardi & Winnick, 2021). We note that output from the 4.0 meq/L simulation results in a shift toward higher groundwater contributions across the watershed, as groundwater has a significantly larger DIC concentration than the 1.0 meq/L simulation (Figure S8 in Supporting Information S1).

4. Discussion

4.1. Alkalinity Controls on CO_2 Concentrations and Fluxes

Across the simulated scenarios, we quantitatively demonstrate how alkalinity alters the equilibration of dissolved CO_2 with the atmosphere in rivers and streams. Increased alkalinity, as previously hypothesized, increases the role of carbonate buffering reactions in maintaining pCO_2 along the stream reach. During active degassing, as shown in Scenarios 1–3, carbonate buffering reactions result in minimally increased atmosphere equilibration timescales, acting to maintain only slightly elevated pCO_2. Notably, however, these timescale increases are minimal and are only in evidence at near-atmospheric pCO_2 values. Further, under conditions in which dissolved CO_2 is actively building up, for example, when local rates of stream corridor respiration or groundwater inputs are higher than degassing rates, carbonate buffering maintains lower pCO_2 concentrations as it actively stores CO_2 as $HCO_3^- + H^+$. This effect is equivalent to the Revelle factor often discussed in the oceanography literature (Broecker et al., 1979; Revelle & Suess, 1957), and has been shown to impact stream CO_2 fluxes (Wang et al., 2021).

In a compilation of US stream data, Stets et al. (2017) showed that systems with high alkalinity tend to exhibit higher pCO_2 at moderate stream scales (discharge of 0.1–6 m^3/s) than systems with low alkalinity. This was hypothesized to reflect carbonate buffering reactions, through their role in maintaining high pCO_2 during downstream degassing. In our modeling exercises, we show that carbonate buffering is unable to explain these observed patterns. In fact, when simulating at the stream network scale, we find that carbonate buffering reactions result in the opposite pattern as observed in the Stets et al. compilation: pCO_2 is slightly elevated in first order streams but is typically lower in 3rd–5th order streams when alkalinity is included, reflecting the increasing importance of stream corridor respiration sources and lower gas exchange velocities that allow generated CO_2 to be stored as $HCO_3^= + H^+$ (Figure 6b).

While beyond the scope of our study, we tentatively suggest that if the observational patterns presented in Stets et al. (2017) are robust, they likely reflect either systematically higher source fluxes (groundwater inputs and/or stream corridor respiration) or systematically lower gas exchange velocities potentially reflecting lower topographic relief (e.g., Rocher-Ros et al., 2019). Regarding elevated source fluxes, we note that Stets et al. (2017) demonstrated lower pCO_2 in the smallest high alkalinity streams which would suggest lower groundwater pCO_2 sources, and we are unaware of a mechanism that would link high alkalinity with higher stream corridor respiration rates. In terms of topography, as high alkalinity typically reflects increased chemical weathering rates often associated with soluble minerals such as carbonates, these landscapes may preferentially exhibit lower gas exchange velocities in higher order streams, resulting in elevated pCO_2 at larger stream scales. To test this hypothesis would require local flow and topographic data, which are not included in the original compilation and may serve as the subject for future work. We also note that our stream network model simulations, in which the only altered variable is alkalinity, are not directly comparable to the US compilation data. For example, we hold groundwater pCO_2 constant, whereas increased alkalinity may be expected to co-occur with reduced groundwater pCO_2 based on chemical weathering reactions that convert CO_2 to alkalinity (e.g., Winnick & Maher, 2018).

We also demonstrate that increasing alkalinity and decreasing groundwater pCO_2 values result in increasing relative contributions of carbonate buffering to total degassing fluxes (Figure 4). Under conditions where groundwater is the sole source of stream pCO_2, carbonate buffering may account for >60% of total degassing fluxes when groundwater has high alkalinity (>4 meq/L) and relatively moderate pCO_2 (<5,000 ppm). These values are consistent with findings in Duvert et al. (2019), where carbonate buffering reactions were shown to support as much as ~60% of total fluxes in a high-alkalinity tropical stream system. While not included in our Figure 4 analysis, proportional carbonate buffering contributions to total fluxes would also decrease if total fluxes increased from stream corridor respiration. Taken together, these findings highlight the importance of accounting for carbonate buffering reactions in budgeting stream network CO_2 fluxes, particularly in high alkalinity (>1 meq/L) systems.

Given these patterns that emerge from our modeling exercises, we expect stream CO_2 spatial patterns and contributions of carbonate buffering to be most observable in stream systems with high alkalinity, relatively low pCO_2 groundwater, and near-atmospheric stream pCO_2. High alkalinity environments generally correspond to the lithologic availability of soluble minerals such as carbonates or mafic silicates present in basalt for groundwater weathering reactions (e.g., Bluth & Kump, 1994; Ibarra et al., 2016). Low groundwater pCO_2 may reflect either terrestrial environments with limited plant productivity or associated organic matter for subsurface respiration (e.g., Calmels et al., 2014), or weathering of soluble minerals that convert groundwater CO_2 to alkalinity (e.g., Winnick & Maher, 2018). Lastly, local instances of near-atmospheric pCO_2 values are observable across all watersheds reflecting high gas exchange velocities and/or low local CO_2 inputs (Rocher-Ros et al., 2019), though stream values and total CO_2 fluxes are generally lower at higher Strahler orders (Butman & Raymond, 2011; Hotchkiss et al., 2015). We also note that these patterns are also applicable to lentic freshwater environments, though beyond the scope of our modeling framework, and may contribute, for example, to observations of CO_2-O_2 relationships that deviate from respiration stoichiometry in high alkalinity lakes (Marcé et al., 2015), similar to the stream diel metabolic dynamics explored Stets et al. (2017).

4.2. Alkalinity Impacts on Carbon Isotope Source Partitioning

In contrast to the effects on CO_2 equilibration timescales, carbonate buffering reactions lead to much longer isotope equilibration timescales for both $\delta^{13}C_{DIC}$ and $\Delta^{14}C_{DIC}$. Mechanistically, this is due to the fact that pCO_2 is buffered only by the proportion of HCO_3^- that does not contribute to alkalinity (CO_2 stored as $HCO_3^- + H^+$). In contrast, the isotopic ratio of DIC is buffered by the entire HCO_3^- and CO_3^{2-} pools, which under high alkalinity are much larger than the CO_2 pool that is actively degassed. As the equilibration timescales for both are regulated by the gas exchange velocity, these larger isotopic buffering results in a much longer equilibration timescale. For example, at an alkalinity of 1 meq/L and initial groundwater pCO_2 of 20,000 ppm, the CO_2 stored as $HCO_3^- + H^+$ is 1.3% the size of the $CO_{2(aq)}$ pool, whereas the full buffering pool of ^{12}C, ^{13}C, and ^{14}C encapsulated in $HCO_3^- + CO_3^{2-}$ is 150% the size of the $CO_{2(aq)}$ pool. Further, a higher proportion of total ^{13}C and ^{14}C are contained within HCO_3^- and CO_3^{2-} relative to ^{12}C due to equilibrium fractionation within the DIC pool. Thus, high alkalinity is more effective at buffering the isotopic composition of DIC, which under high alkalinity conditions does not equilibrate until almost all of the net CO_2 degassing has already occurred. At the stream network scale, this results in stream $\delta^{13}C_{DIC}$ and $\Delta^{14}C_{DIC}$ that are much less sensitive to sub-reach changes in topography and source inputs that can dramatically alter pCO_2 over small scales. While these results have been demonstrated indirectly through the application of similar models to groundwater degassing (e.g., Venkiteswaran et al., 2014) and have been noted observationally for ^{14}C (Bourke et al., 2014), this study is the first to directly quantify these timescales for both $\delta^{13}C_{DIC}$ and $\Delta^{14}C_{DIC}$.

These differences in the magnitude impacts of buffering dynamics on pCO_2 versus carbon isotopes greatly complicate methods of CO_2 source evaluation. The size of the isotope buffering pool along with degassing from the CO_2 pool, which has a lower isotopic value than DIC effectively acts to decouple variations between carbon concentrations (pCO_2 or DIC) and isotopic composition ($\delta^{13}C_{DIC}$ or $\Delta^{14}C_{DIC}$). During degassing, the bulk of the isotopic change occurs after pCO_2 has equilibrated with the atmosphere, which makes measurements of covariation analytically difficult. More importantly, in situations where CO_2 (and DIC) is building up rather than degassing, $\delta^{13}C_{DIC}$ or $\Delta^{14}C_{DIC}$ is largely insensitive to these new inputs via this hysteresis. This results in reach-scale patterns in which $\delta^{13}C_{DIC}$ and pCO_2 are largely decoupled and deviate significantly from the overall degassing pattern, as shown in Figure 7. Typical isotopic source evaluation methods either employ linear mixing models of pCO_2 or DIC and $\delta^{13}C_{DIC}$ (e.g., Campeau et al., 2017, 2018) or degassing models (Venkiteswaran et al., 2014). The assumptions underlying both of these methods are that pCO_2 and $\delta^{13}C_{DIC}$ co-vary systematically across a given study area. We show that this is not the case; carbonate buffering acts to decouple pCO_2 and $\delta^{13}C_{DIC}$ patterns in all but the 1st order headwaters that are dominated by groundwater seep degassing patterns. This decoupling occurs even at low and moderate alkalinity values (0.1 meq/L shown in Figure S7 of the Supporting Information S1; 1 meq/L shown in Figure 7). Therefore, studies that utilize pCO_2- or DIC- $\delta^{13}C_{DIC}$ methods for evaluating carbon sources are only accurate under very low alkalinity conditions or in directly evaluating groundwater seep degassing trends in spring-fed headwaters.

Despite the factors that complicate the relationships between isotope composition and $p\mathrm{CO}_2$, our modeling simulations suggest a useful path forward. Specifically, $\delta^{13}\mathrm{C}_{\mathrm{DIC}}$ and $\Delta^{14}\mathrm{C}_{\mathrm{DIC}}$ both represent the full DIC pool and have equilibration timescales that are similarly impacted by alkalinity. Therefore, they may be used to partition DIC sources more directly through end-member mixing analyses. Furthermore, the increased equilibration timescales in high alkalinity systems mean that point measurements of $\delta^{13}\mathrm{C}_{\mathrm{DIC}}$ and $\Delta^{14}\mathrm{C}_{\mathrm{DIC}}$ are more integrative of upstream conditions and may provide useful insight into broader spatial trends than $p\mathrm{CO}_2$, which can often vary over scales of 10's of meters (e.g., Johnson et al., 2008). Paired $\delta^{13}\mathrm{C}_{\mathrm{DIC}}$ and $\Delta^{14}\mathrm{C}_{\mathrm{DIC}}$ measurements may be particularly useful for DIC source partitioning in systems where groundwater DIC is controlled by carbonate mineral weathering reactions, such as watersheds with limestone or shale bedrock. Under these conditions and as parameterized across our simulations, groundwater, stream corridor respiration, and the atmosphere all represent unique end-members in $\delta^{13}\mathrm{C}_{\mathrm{DIC}} - \Delta^{14}\mathrm{C}_{\mathrm{DIC}}$ space (e.g., Table 1). We note that Sveinbjörnsdóttir et al. (2020) have previously employed paired $\delta^{13}\mathrm{C}_{\mathrm{DIC}} - \Delta^{14}\mathrm{C}_{\mathrm{DIC}}$ to evaluate DIC sources; however, they used a linear end-member mixing model, which our results show neglects non-linear variations between $\delta^{13}\mathrm{C}_{\mathrm{DIC}}$ and $\Delta^{14}\mathrm{C}_{\mathrm{DIC}}$ degassing rates and may therefore only be accurate under low alkalinity conditions.

In our simulations, we calculated the contributions of groundwater versus stream corridor respiration to DIC using simulated $\delta^{13}\mathrm{C}_{\mathrm{DIC}} - \Delta^{14}\mathrm{C}_{\mathrm{DIC}}$ relationships. At any given simulated stream point, measured values represent the integration of upstream processes at the spatial scale dependent on stream velocity, gas exchange velocity, and the alkalinity-dependent equilibration timescales of carbon isotope values. We propose that these methods may be employed within field systems, which requires the characterization of end-member source $\delta^{13}\mathrm{C}_{\mathrm{DIC}} - \Delta^{14}\mathrm{C}_{\mathrm{DIC}}$ values, along with alkalinity measurements to calculate contour mixing lines (see Supporting Information S1 for example code). Currently, methods for estimating source contributions within a stream reach are intensive, and typically involve calculating stream corridor metabolic rates through DO sensor deployment and absolute CO_2 fluxes through high resolution sampling (e.g., Hotchkiss et al., 2015). While $\Delta^{14}\mathrm{C}_{\mathrm{DIC}}$ measurements are costly, this method has the advantage of allowing for rapid characterization of source partitioning across watershed scales, through sampling campaigns that target multiple streams. These may be particularly useful, for example, for targeting spatial variability and Strahler order scale dependencies in stream carbon sources at a point in time, such as during a storm event or peak snowmelt. Traditionally, source characterization across stream orders within a watershed would require the redeployment of DO sensors at each new stream reach, whereas this method would allow for a larger spatial characterization at a given timepoint by taking representative samples from a set of stream reaches assuming relatively consistent end-member sources across the watershed.

4.3. Model Limitations

While these models are meant to be broadly representative of the processes controlling atmospheric equilibration of river and stream waters, there are a number of assumptions we have made that must be validated on a site-by-site basis for direct data comparisons. First, our simulations parameterize stream corridor metabolism as net respiration rather than separately simulating photosynthesis and respiration. This parameterization assumes that organic matter derived from terrestrial materials is the same as that synthesized in the stream, such that stream corridor photosynthesis and respiration have equal and opposite impacts on the isotopic composition. This assumption may be violated, for example, in sites where terrestrially-derived DOC represents C_4 plant matter, and at the field-scale, measurements of distinct isotopic end-members for different DOC sources are needed to evaluate this assumption. To simulate diel variations in the carbonate system, the model would likely need to be amended to parameterize photosynthesis and the associated fractionation independently, as opposed to our net respiration representation.

As stated throughout the manuscript, we also neglect processes that alter alkalinity concentrations, which may include anaerobic respiration, calcite precipitation, and spatiotemporal changes in groundwater chemistry. We similarly neglect CO_2 generation from methane oxidation that may result in distinctly low $\delta^{13}\mathrm{C}_{\mathrm{DIC}}$ values. We assume that there is no kinetic fractionation associated with CO_2 degassing from turbulent exchange, and that apparent fractionation during degassing reflects only equilibration with the elevated atmospheric values of $\delta^{13}\mathrm{C}_{\mathrm{DIC}}$ and $\Delta^{14}\mathrm{C}_{\mathrm{DIC}}$. We feel that this issue remains an open question that has not been directly addressed in stream environments, though our modeling framework is flexible to incorporate it as a specified kinetic fractionation factor when molecular diffusion is a significant factor in degassing rates (e.g., Zhang et al., 1995). Lastly, for simplicity, we have kept temperatures constant throughout this analysis. Temperature changes would impact results via $CO_{2(aq)}$ solubility as well as equilibrium constants and associated equilibrium fractionation within the carbonate system presented in Table 1, which can be manually altered within the model.

5. Conclusions

Given the recent recognition of carbonate buffering reactions as an important control on spatial patterns of CO_2 concentrations and fluxes in stream systems, we developed a non-dimensional reactive transport framework for evaluating their impacts on atmospheric equilibration of dissolved inorganic carbon. We find that while carbonate buffering does increase the timescales over which $p\mathrm{CO}_2$ approaches steady-state values, these changes are relatively small and cannot explain observations of elevated $p\mathrm{CO}_2$ at increasing spatial scales in high alkalinity versus low alkalinity systems. This increase in equilibration timescale, along with increased contributions of carbonate buffering reactions to total CO_2 fluxes, depends on the size of the buffering reservoir (or amount of CO_2 stored as $HCO_3^- + H^+$) relative to $CO_{2(aq)}$, such that carbonate buffering reactions contribute a larger proportion of CO_2 fluxes as alkalinity increases and groundwater $p\mathrm{CO}_2$ decreases. In contrast to CO_2, the isotopic composition of DIC is buffered by the entire DIC pool as CO_2 equilibrates with the atmosphere, which is much larger than the pool of CO_2 stored as $HCO_3^- + H^+$. As a result, isotopic equilibration timescales are much more sensitive to stream alkalinity, with $\delta^{13}C_{DIC}$ and $\Delta^{14}C_{DIC}$ increasing by ~2 orders of magnitude relative to CO_2 timescales. The result of this mismatch in timescales is that under moderate alkalinity conditions, isotope composition becomes largely decoupled from $p\mathrm{CO}_2$, rendering typical methods for CO_2 source tracing ineffective. We show, however, that due to similar impacts on equilibration timescales, paired $\delta^{13}C_{DIC}$ and $\Delta^{14}C_{DIC}$ measurements may be effective tracers of groundwater versus stream corridor respiration sources of DIC in environments where groundwater DIC is controlled by carbonate weathering reactions, typical of moderate to high alkalinity systems. Taken together, we present a generalizable framework for quantifying and interpreting the role of carbonate buffering reactions in stream CO_2 dynamics and develop a new potential method for utilizing the isotopic composition of DIC to trace stream carbon sources.

Data Availability Statement

All code used in this work is available in Supporting Information S1. This code is also available publicly via the open-source Hydroshare platform in Winnick (2023), https://www.hydroshare.org/resource/2a2132999fb84214aad0596783812db2/.

Acknowledgments
We thank Stephen Burns and Berry Williams for useful discussions about the carbon isotope modeling. We thank Mark Torres, two anonymous reviewers, and the Associate Editor for comments that improved an earlier version of this manuscript. This work was supported by the NSF awards EAR-2103520 and EAR-2318056 to MJW.

References

Bluth, G. J. S., & Kump, L. R. (1994). Lithologic and climatologic controls of river chemistry. *Geochimica et Cosmochimica Acta*, *58*(10), 2341–2359. https://doi.org/10.1016/0016-7037(94)90015-9

Bourke, S. A., Harrington, G. A., Cook, P. G., Post, V. E., & Dogramaci, S. (2014). Carbon-14 in streams as a tracer of discharging groundwater. *Journal of Hydrology*, *519*, 117–130. https://doi.org/10.1016/j.jhydrol.2014.06.056

Broecker, W. S., Takahashi, T., Simpson, H. J., & Peng, T.-H. (1979). Fate of fossil fuel carbon dioxide and the global carbon budget. *Science*, *206*(4417), 409–418. https://doi.org/10.1126/science.206.4417.409

Butman, D., & Raymond, P. A. (2011). Significant efflux of carbon dioxide from streams and rivers in the United States. *Nature Geoscience*, *4*(12), 839–842. https://doi.org/10.1038/ngeo1294

Calmels, D., Gaillardet, J., & François, L. (2014). Sensitivity of carbonate weathering to soil CO_2 production by biological activity along a temperate climate transect. *Chemical Geology*, *390*, 74–86. https://doi.org/10.1016/j.chemgeo.2014.10.010

Campeau, A., Bishop, K., Nilsson, M. B., Klemedtsson, L., Laudon, H., Leith, F. I., et al. (2018). Stable carbon isotopes reveal soil-stream DIC linkages in contrasting headwater catchments. *Journal of Geophysical Research: Biogeosciences*, *123*(1), 149–167. https://doi.org/10.1002/2017JG004083

Campeau, A., Wallin, M. B., Giesler, R., Löfgren, S., Mörth, C.-M., Schiff, S., et al. (2017). Multiple sources and sinks of dissolved inorganic carbon across Swedish streams, refocusing the lens of stable C isotopes. *Scientific Reports*, *7*(1), 9158. https://doi.org/10.1038/s41598-017-09049-9

Carroll, R. W. H., Bearup, L. A., Brown, W., Dong, W., Bill, M., & Willlams, K. H. (2018). Factors controlling seasonal groundwater and solute flux from snow-dominated basins. *Hydrological Processes*, *32*(14), 2187–2202. https://doi.org/10.1002/hyp.13151

Cole, J. J., Prairie, Y. T., Caraco, N. F., McDowell, W. H., Tranvik, L. J., Striegl, R. G., et al. (2007). Plumbing the global carbon cycle: Integrating inland waters into the terrestrial carbon budget. *Ecosystems*, *10*(1), 172–185. https://doi.org/10.1007/s10021-006-9013-8

Cole, T. L., Torres, M. A., & Kemeny, P. C. (2022). The hydrochemical signature of incongruent weathering in Iceland. *Journal of Geophysical Research: Earth Surface*, *127*(6), e2021JF006450. https://doi.org/10.1029/2021JF006450

DelSontro, T., Beaulieu, J. J., & Downing, J. A. (2018). Greenhouse gas emissions from lakes and impoundments: Upscaling in the face of global change. *Limnology and Oceanography Letters*, *3*(3), 64–75. https://doi.org/10.1002/lol2.10073

Drake, T. W., Raymond, P. A., & Spencer, R. G. M. (2018). Terrestrial carbon inputs to inland waters: A current synthesis of estimates and uncertainty. *Limnology and Oceanography Letters*, *3*(3), 132–142. https://doi.org/10.1002/lol2.10055

Druhan, J. L., Guillon, S., Lincker, M., & Arora, B. (2021). Stable and radioactive carbon isotope partitioning in soils and saturated systems: A reactive transport modeling benchmark study. *Computational Geosciences*, *25*(4), 1393–1403. https://doi.org/10.1007/s10596-020-09937-6

Duvert, C., Bossa, M., Tyler, K. J., Wynn, J. G., Munksgaard, N. C., Bird, M. I., et al. (2019). Groundwater-derived DIC and carbonate buffering enhance fluvial CO_2 evasion in two Australian tropical rivers. *Journal of Geophysical Research: Biogeosciences*, *124*(2), 312–327. https://doi.org/10.1029/2018JG004912

Friedlingstein, P., O'Sullivan, M., Jones, M. W., Andrew, R. M., Gregor, L., Hauck, J., et al. (2022). Global carbon budget 2022. *Earth System Science Data*, *14*(11), 4811–4900. https://doi.org/10.5194/essd-14-4811-2022

Gómez-Gener, L., Rocher-Ros, G., Battin, T., Cohen, M. J., Dalmagro, H. J., Dinsmore, K. J., et al. (2021). Global carbon dioxide efflux from rivers enhanced by high nocturnal emissions. *Nature Geoscience*, *14*(5), 289–294. https://doi.org/10.1038/s41561-021-00722-3

Grant, S. B., Azizian, M., Cook, P., Boano, F., & Rippy, M. A. (2018). Factoring stream turbulence into global assessments of nitrogen pollution. *Science*, *359*(6381), 1266–1269. https://doi.org/10.1126/science.aap8074

Hotchkiss, E. R., Hall, R. O., Jr., Sponseller, R. A., Butman, D., Klaminder, J., Laudon, H., et al. (2015). Sources of and processes controlling CO_2 emissions change with the size of streams and rivers. *Nature Geoscience*, *8*(9), 696–699. https://doi.org/10.1038/ngeo2507

Ibarra, D. E., Caves, J. K., Moon, S., Thomas, D. L., Hartmann, J., Chamberlain, C. P., & Maher, K. (2016). Differential weathering of basaltic and granitic catchments from concentration–discharge relationships. *Geochimica et Cosmochimica Acta*, *190*, 265–293. https://doi.org/10.1016/j.gca.2016.07.006

Izagirre, O., Agirre, U., Bermejo, M., Pozo, J., & Elosegi, A. (2008). Environmental controls of whole-stream metabolism identified from continuous monitoring of Basque streams. *Journal of the North American Benthological Society*, *27*(2), 252–268. https://doi.org/10.1899/07-022.1

Johnson, M. S., Lehmann, J., Riha, S. J., Krusche, A. V., Richey, J. E., Ometto, J. P. H. B., & Couto, E. G. (2008). CO_2 efflux from Amazonian headwater streams represents a significant fate for deep soil respiration. *Geophysical Research Letters*, *35*(17), L17401. https://doi.org/10.1029/2008GL034619

Jungkunst, H. F., Flessa, H., Scherber, C., & Fiedler, S. (2008). Groundwater level controls CO_2, N_2O and CH_4 fluxes of three different hydromorphic soil types of a temperate forest ecosystem. *Soil Biology and Biochemistry*, *40*(8), 2047–2054. https://doi.org/10.1016/J.SOILBIO.2008.04.015

Kessler, T. J., & Harvey, C. F. (2001). The global flux of carbon dioxide into groundwater. *Geophysical Research Letters*, *28*(2), 279–282. https://doi.org/10.1029/2000GL011505

Kirk, L., & Cohen, M. J. (2023). River corridor sources dominate CO_2 emissions from a lowland river network. *Journal of Geophysical Research: Biogeosciences*, *128*(1), e2022JG006954. https://doi.org/10.1029/2022JG006954

Lauerwald, R., Allen, G. H., Deemer, B. R., Liu, S., Maavara, T., Raymond, P., et al. (2023). Inland water greenhouse gas budgets for RECCAP2: 1. State-of-the-art of global scale assessments. *Global Biogeochemical Cycles*, *37*(5), e2022GB007657. https://doi.org/10.1029/2022GB007657

Marcé, R., Obrador, B., Morguí, J.-A., Lluís Riera, J., López, P., & Armengol, J. (2015). Carbonate weathering as a driver of CO_2 supersaturation in lakes. *Nature Geoscience*, *8*(2), 107–111. https://doi.org/10.1038/ngeo2341

Polsenaere, P., & Abril, G. (2012). Modelling CO_2 degassing from small acidic rivers using water pCO_2, DIC and δ^{13}C-DIC data. *Geochimica et Cosmochimica Acta*, *91*, 220–239. https://doi.org/10.1016/j.gca.2012.05.030

Raymond, P. A., Hartmann, J., Lauerwald, R., Sobek, S., McDonald, C., Hoover, M., et al. (2013). Global carbon dioxide emissions from inland waters. *Nature*, *503*(7476), 355–359. https://doi.org/10.1038/nature12760

Revelle, R., & Suess, H. E. (1957). Carbon dioxide exchange between atmosphere and ocean and the question of an increase of atmospheric CO_2 during the past decades. *Tellus*, *9*(1), 18–27. https://doi.org/10.1111/j.2153-3490.1957.tb01849.x

Rocher-Ros, G., Sponseller, R. A., Lidberg, W., Mörth, C.-M., & Giesler, R. (2019). Landscape process domains drive patterns of CO_2 evasion from river networks. *Limnology and Oceanography Letters*, *4*(4), 87–95. https://doi.org/10.1002/lol2.10108

Saccardi, B., & Winnick, M. (2021). Improving predictions of stream CO_2 concentrations and fluxes using a stream network model: A case study in the East River Watershed, CO, USA. *Global Biogeochemical Cycles*, *35*(12), e2021GB006972. https://doi.org/10.1029/2021GB006972

Sawakuchi, H. O., Neu, V., Ward, N. D., de Barros, M. L. C., Valerio, A. M., Gagne-Maynard, W., et al. (2017). Carbon dioxide emissions along the lower Amazon River. *Frontiers in Marine Science*, *4*. https://doi.org/10.3389/fmars.2017.00076

Stets, E. G., Butman, D., McDonald, C. P., Stackpoole, S. M., DeGrandpre, M. D., & Striegl, R. G. (2017). Carbonate buffering and metabolic controls on carbon dioxide in rivers. *Global Biogeochemical Cycles*, *31*(4), 663–677. https://doi.org/10.1002/2016GB005578

Sveinbjörnsdóttir, Á. E., Stefánsson, A., Heinemeier, J., Arnórsson, S., Eiríksdóttir, E. S., & Ólafsdóttir, R. (2020). Assessing the sources of inorganic carbon in surface-soil- and non-thermal groundwater in Iceland by δ^{13}C and ^{14}C. *Geochimica et Cosmochimica Acta*, *279*, 165–188. https://doi.org/10.1016/j.gca.2020.03.021

Ulseth, A. J., Hall, R. O., Boix Canadell, M., Madinger, H. L., Niayifar, A., & Battin, T. J. (2019). Distinct air–water gas exchange regimes in low- and high-energy streams. *Nature Geoscience*, *12*(4), 259–263. https://doi.org/10.1038/s41561-019-0324-8

Venkiteswaran, J. J., Schiff, S. L., & Wallin, M. B. (2014). Large carbon dioxide fluxes from headwater boreal and sub-boreal streams. *PLoS One*, *9*(7), e101756. https://doi.org/10.1371/journal.pone.0101756

Wang, C., Xie, Y., Liu, S., McCallum, J. L., Li, Q., & Wu, J. (2021). Effects of diffuse groundwater discharge, internal metabolism and carbonate buffering on headwater stream CO_2 evasion. *Science of the Total Environment*, *777*, 146230. https://doi.org/10.1016/j.scitotenv.2021.146230

Winnick, M. (2023). *Supplementary data for Winnick and Saccardi—Impacts of carbonate buffering on atmospheric equilibration of CO_2, δ^{13}CDIC, and Δ^{14}CDIC in rivers and streams*. HydroShare. Retrieved from http://www.hydroshare.org/resource/2a2132999fb84214aad0596783812db2

Winnick, M. J. (2021). Stream transport and substrate controls on nitrous oxide yields from hyporheic zone denitrification. *AGU Advances*, *2*(4), e2021AV000517. https://doi.org/10.1029/2021AV000517

Winnick, M. J., Carroll, R. W. H., Williams, K. H., Maxwell, R. M., Dong, W., & Maher, K. (2017). Snowmelt controls on concentration-discharge relationships and the balance of oxidative and acid-base weathering fluxes in an alpine catchment, East River, Colorado. *Water Resources Research*, *53*(3), 2507–2523. https://doi.org/10.1002/2016WR019724

Winnick, M. J., Lawrence, C. R., McCormick, M., Druhan, J. L., & Maher, K. (2020). Soil respiration response to rainfall modulated by plant phenology in a Montane Meadow, East River, Colorado, USA. *Journal of Geophysical Research: Biogeosciences*, *125*(10), e2020JG005924. https://doi.org/10.1029/2020JG005924

Winnick, M. J., & Maher, K. (2018). Relationships between CO_2, thermodynamic limits on silicate weathering, and the strength of the silicate weathering feedback. *Earth and Planetary Science Letters*, *485*, 111–120. https://doi.org/10.1016/j.epsl.2018.01.005

Zhang, J., Quay, P. D., & Wilbur, D. O. (1995). Carbon isotope fractionation during gas-water exchange and dissolution of CO_2. *Geochimica et Cosmochimica Acta*, *59*(1), 107–114. https://doi.org/10.1016/0016-7037(95)91550-D